






Guide-Wired Helical Microrobot for Percutaneous Revascularization in Chronic Total Occlusion *In-Vivo* Validation

Kim Tien Nguyen , Seok-Jae Kim, Huyn-Ki Min, Manh Cuong Hoang , Gwangjun Go, Byungjeon Kang , Jayoung Kim, Eunpyo Choi, Ayoung Hong , *Member, IEEE*, Jong-Oh Park, *Member, IEEE*, and Chang-Sei Kim , *Member, IEEE*

Abstract—Objective: For the revascularization in small vessels such as coronary arteries, we present a guide-wired helical microrobot mimicking the corkscrew motion for mechanical atherectomy that enables autonomous therapeutics and minimizing the radiation exposure to clinicians. **Methods:** The microrobot is fabricated with a spherical joint and a guidewire. A previously developed external electromagnetic manipulation system capable of high power and frequency is incorporated and an autonomous guidance motion control including driving and steering is implemented in the prototype. We tested the validity of our approach in animal experiments under clinical settings. For the *in vivo* test, artificial thrombus was fabricated and placed in a small vessel and atherectomy procedures were conducted. **Results:** The devised approach enables us to navigate the helical robot to the target area and successfully unclog the thrombosis in rat models *in vivo*. **Conclusion:** This technology overcomes several limitations associated with a small vessel environment and promises to advance medical microrobotics for real clinical applications while achieving intact operation and minimizing radiation exposures to clinicians. **Significance:** Advanced microrobot based on multi-discipline technology could be validated *in vivo* for the first time and that may foster the microrobot application at clinical sites.

Index Terms—Cardiovascular therapeutics, electromagnetic navigation system, Helical microrobot, mechanical atherectomy, percutaneous coronary intervention.

Manuscript received July 19, 2020; revised September 21, 2020 and November 24, 2020; accepted December 17, 2020. Date of publication December 22, 2020; date of current version July 19, 2021. This work was supported by a grant of the Korea Health Technology Development R&D Project through the Korea Health Industry Development Institute (KHIDI), funded by the Ministry of Health & Welfare, Republic of Korea under Grant HI19C0642. (Corresponding authors: Jong-Oh Park; Chang-Sei Kim.)

Kim Tien Nguyen, Manh Cuong Hoang, Gwangjun Go, and Eunpyo Choi are with the School of Mechanical Engineering, Chonnam National University.

Byungjeon Kang and Ayoung Hong are with the College of AI Convergence, Chonnam National University.

Seok-Jae Kim, Huyn-Ki Min, and Jayoung Kim are with the Korea Institute of Medical Microrobotics.

Jong-Oh Park is with the Korea Institute of Medical Microrobotics, Gwangju 61011, South Korea (e-mail: jop@jnu.ac.kr).

Chang-Sei Kim is with the School of Mechanical Engineering, Chonnam National University, Gwangju 61186, South Korea (e-mail: ckim@jnu.ac.kr).

This article has supplementary downloadable material available at <https://doi.org/10.1109/TBME.2020.3046513>, provided by the authors.

Digital Object Identifier 10.1109/TBME.2020.3046513

I. INTRODUCTION

CHRONIC total occlusion (CTO) is a common complication of coronary artery disease (CAD) [1] and peripheral arterial occlusive disease (PAD) [2]. Approximately one-third of the CAD patients and up to 40% of the PAD patients develop CTO. As a minimally invasive procedure to treat CTO, percutaneous intervention is commonly used and has benefits of patient comfort and short recovery time [3], [4]. In which, reperfusion therapy that removes the obstacles in the vessel and restores the blood flow is one of the critical operations in the procedure: it is important to salvage occluded vessels and remove thrombi or infarcted plaques without damaging.

Mechanical thrombectomy and atherectomy devices have been used for reperfusion therapy in vessels [2]. For example, mechanical thrombectomy for acute total occlusions involves corkscrew distal wires [5], balloon angioplasty [6], stent retrievers [7], and direct aspiration [8]. Atherectomy includes the use of rotational and directional cutting tips or laser ablation [2] via catheterization for percutaneous coronary intervention (PCI) and peripheral arteries. The Rotablator system has been used for the treatment of CTO over the past 30 years owing to its simple design of a rotary diamond-coated burr connected to a flexible shaft driven by an air turbine [9], [10]. Other catheters equipped with rotational helical tips, such as Jetstream system [11], Wildcat catheter [12], Rotarex [13], [14], and Silverhawk plaque excision system [15] have been also reported to offer a moderately higher success rate in the removal of severely calcified lesions in peripheral vessels. The above-mentioned devices are effective in treating atherosclerosis in large vessels [2], [11]. However, employing such devices for small vessel treatment is still challenging due to the physical size of the instruments. Another disadvantage for the current system is that the catheters or the guidewires are manually operated by clinicians: this results in the outcomes of the procedure being highly dependent on the skills and experiences of clinicians and there exists the risks of radiation exposure and orthopedic injuries to the operators [16]–[18].

To cope with the challenges of conventional PCI, the robot-assisted PCI (R-PCI) have emerged. The operator can remotely control the intravascular therapeutics device in a radiation shield room by using interventional cockpit systems such as CorPath

200 (Corindus Vascular Robotics, MA, USA) [19] and R-One (RoboCath, France) [20]. The R-PCI was associated with almost 50% lower risk of major procedural complications compared with the traditional method [21]. However, the R-PCI still has a limitation of manual access of the catheter into the vessels and difficulty against hard-calcified lesions [22].

Alternatively, an automated magnetic guidewire controlled by an electromagnetic navigation system (ENS) composed of an electromagnetic actuator (EMA) and imaging devices, such as optical cameras, angiography, and ultrasound imaging, was introduced. The system is considered as a promising approach because it can remotely control multiple degrees of freedom motion, enables the use of millimeter- and micrometer-sized devices, has a high actuation force, and is relatively cheap [23]–[32]. Several ENS demonstrated the practical applicability in clinical sites such as Niobe (Stereotaxis Inc., USA) [24], [25], CGCI (Magnetecs, USA) [26], [27], Amigo (Catheter Robotics Inc., USA) [28], [29], Sensei (Hansen Medical Inc., USA) [30], [31], and Aeon Phocus (Aeon Scientific, Switzerland) [32]. In the ENS, a magnetically driven guidewire equipped with a small permanent magnet [24], [33]–[37] or an electromagnetic coil [23], [38] at the guidewire tip was incorporated. Based on these systems, forward-backward motions of a sharp-tip were utilized to break clots through a motorized feeding device [33]. However, the clot removal by using this simple motion was not effective and the risk of vessel perforation was high [39].

A magnetic helical microrobot has been researched for the effective revascularization in the ENS, since it can achieve both locomotion and drilling without embodied actuators [40]–[43]. The microrobot is actuated by converting electromagnetic torque into propulsion force through external rotating magnetic fields. Here, a high-frequency alternating electromagnetic field is required to generate stable locomotion and strong drilling force to overcome blood flow and pressure influences in the vessel, in addition to safe retractions. Ultimately, the movement and the drilling performance in the *in vivo* environments need to be validated for practical percutaneous revascularization.

To address these issues, we present a guide-wired helical microrobot (GHM) for percutaneous revascularization to reinstate blood flow in narrow vessels with *in vivo* validation in the rat model. The overall schematic of the proposed system by considering further clinical installation is illustrated in Fig. 1. Our approach unified a bio-inspired helical microrobot, small-scale robot fabrications, and autonomous navigation systems integrated with an ENS. The EMA is based on our previous work [40], in which we presented a resonance control system capable of high frequency and powered electromagnetic field generation. The GHM with a micro-fabricated spherical joint is connected to a clinically available guidewire for safe retraction. The GHM can achieve mechanical revascularization via drilling as well as steering and propelling against the strong blood flow in vessels. We demonstrate the performance of the GHM in rats with artificial blockages mimicking the CTO in humans.

The paper is organized as follows. Section II presents design and fabrication of the GHM. Section III presents the control strategy and the performance validation in both *in-vitro* and

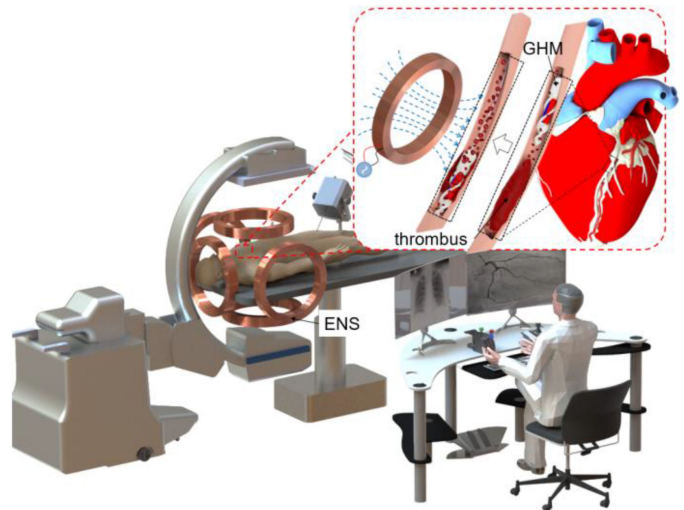


Fig. 1. Conceptual schematic of thrombus removal using the GHM. The GHM is navigated toward the target in the steering mode, after which an alternative magnetic field is applied to generate powerful drilling to break the thrombus.

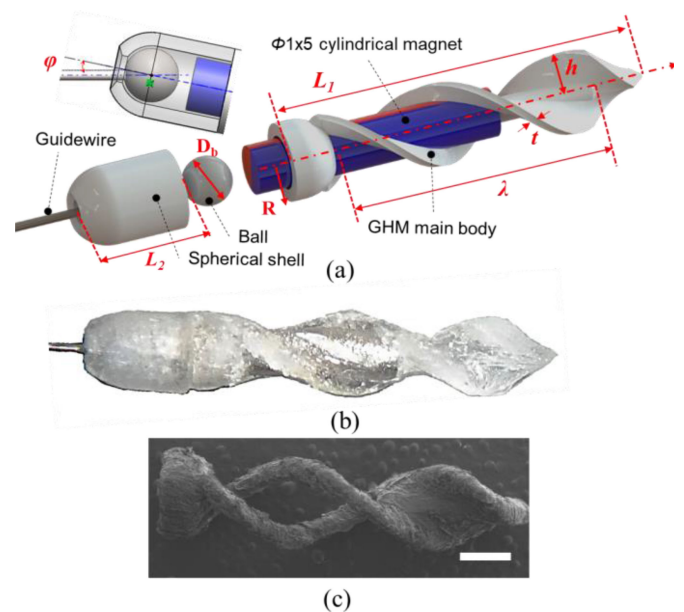


Fig. 2. Design and fabrication of GHM. (a) Structural design of the GHM. (b) 3D-printed GHM. (c) Scanning electron microscopy image of the main body. Scale bar: 1 mm.

in-vivo environments are shown in Section IV. Section V provides conclusions and future works for further clinical applications.

II. DESIGN AND FABRICATION OF GHM

A. Design of the GHM

Fig. 2(a) presents the structure of the GHM, and Fig. 2(b) depicts the fabricated prototype and a scanned electron microscopic image of the main body. Considering the physiological

TABLE I
GEOMETRIC PARAMETERS OF THE GHM

| Symbol | Dimensions | Description |
|------------------|--------------------|------------------------|
| R | 0.8 mm | Body radius |
| λ | 5.5 mm | Pitch length |
| t | 0.2 mm | Spiral thickness |
| h | 0.6 mm | Spiral height |
| L_1 | 7.5 mm | Main body length |
| $L_m \times D_m$ | 1 mm \times 5 mm | Permanent magnet |
| D_b | 1 mm | Ball diameter |
| L_2 | 2 mm | Spherical shell length |
| φ | $\pm 3^\circ$ | Free bending angle |

coronary artery size (normally varying between 1.6 mm and 4.5 mm [44]), the body diameter of the GHM was designed to be 1.6 mm. The GHM could be inserted into small vessels through a commercially available catheter. The spiral-shaped main body of the helical microrobot includes an inner space to fix a cylindrical permanent magnet (NdFeB, N52, JL magnet, Korea), which can interact with the external electromagnetic actuator. The microrobot comprises a sharp tip that exerts punching motions at the target region. To achieve both drilling and steering using a single magnet, the magnetization direction of the magnet was selected to be perpendicular to the body axis. This also maximized the drilling torque. The proposed device was equipped with a micro spherical joint at the end of the robot body. At this joint, a ball was connected to a clinically available guidewire, called the super-elastic Nitinol guidewire (\varnothing 0.152 mm, Confluent Medical Technologies, USA), which was placed inside the spherical joint shell. The spherical joint resulted in two free rotations along with both axial and colatitude directions simultaneously. The axial directional rotation along with the robot body length enabled helical rotations with respect to the fixed guidewire, which was eventually performed for drilling into the thrombus. The colatitude directional rotation perpendicular to the axial direction of the robot provided free bending between the tip and guidewire, which enabled the GHM to steer toward the desired direction. The maximum free bending angle, φ , was set to 10° , as shown in Fig. 2(a). The guidewire resulted in a stronger resisting force against blood flow while approaching the target thrombus. This ultimately led to stable robot motion as well as easy and safe retrieval of the device after completion of the procedure. Table I summarizes the geometric parameters of the designed GHM.

B. Fabrication of the GHM

The components of the GHM, including the helical shaped body, a ball housing, and a spherical joint, were designed with computer-aided design software (Solidworks, Dassault Systèmes, USA) and constructed using a photopolymer jetting 3D printer (Object Eden260VS, Stratasys, USA) with a transparent material (VeroClear-RGD810, Stratasys, USA). The maximum free bending angle after fabrication was limited to 3° due to the limited 3D printing resolution and fabrication errors. The final model of the GHM body featured a total length of 9.5 mm (excluding the length of the guidewire) and a diameter of 1.6 mm.

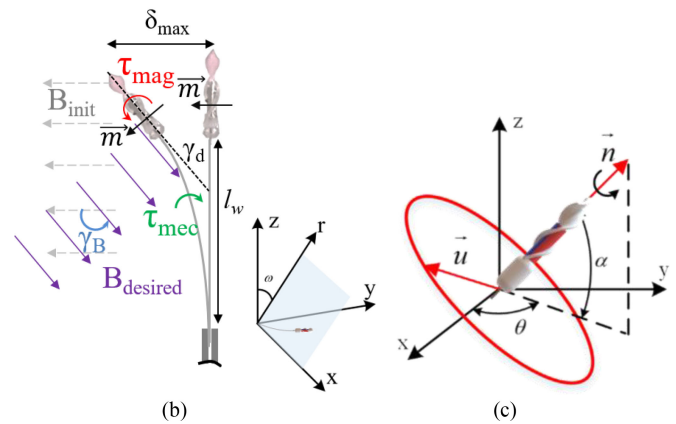
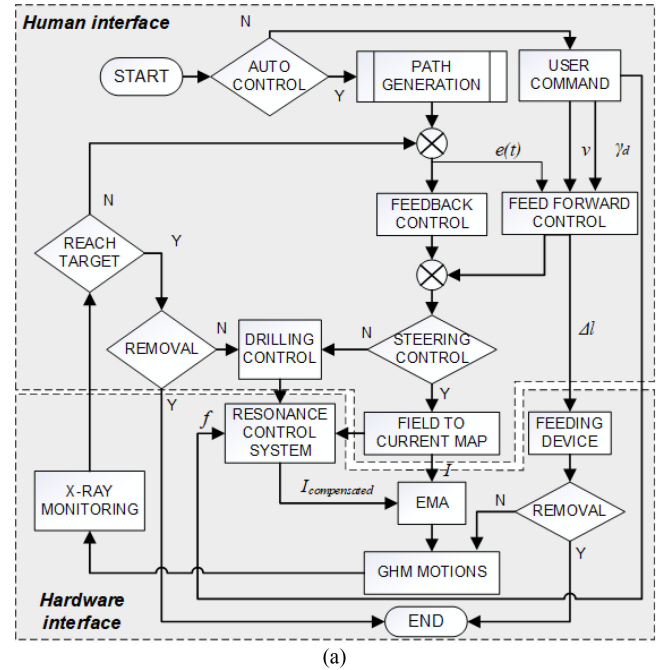


Fig. 3. Magnetic steering and drilling control of the GHM. (a) Block diagram of the control system for the GHM. (b) Steering of the GHM under electromagnetic control (c). Drilling control of the GHM under the desired rotating field.

III. ACTUATION OF THE GHM

The block diagram of the steering and driving control for the GHM is depicted in Fig. 3(a). The designed system employs a static uniform magnetic field for steering and a rotating magnetic field for drilling. The external actuation of the GHM was designed based on Maxwell's magnetic field principle, on which depending on the applied field, the magnetic torque acting on the GHM tends to align the magnetic moment of the permanent magnet in the GHM, m , to create the bending and drilling motions, as expressed below:

$$\tau_{mag} = m \times B \quad (1)$$

where B is the resultant magnetic flux density generated by the external electromagnetic coils.

For steering control, the magnetic torque can be rewritten in form of:

$$\tau_{mag} = mB \sin(\gamma_B - \gamma_d) \quad (2)$$

where γ_d is the desired steering angle of the GHM measured from the initial direction of the GHM. γ_B is the angle of external magnetic field measured from the initial field (B_{init}) which was set at 90° to align the GHM at 0° (shown in Fig. 3b) due to the perpendicular of magnetization direction of the magnet and its body's axis. A uniform magnetic field was set to an angle of 90° away from the desired direction to maximize the bending torque ($\gamma_B - \gamma_d = 90^\circ$). The required magnetic field (denoted by the purple arrows in Fig. 3(b)) for a specific steering angle is calculated by equalizing the induced magnetic torque, τ_{mag} , and the mechanical restoring torque, τ_{mec} , as follows:

$$B_{desired} = \frac{EI \tan(\gamma_d - \varphi)}{ml_w} \quad (3)$$

As shown in Fig. 3(c), the desired rotating field generated in a plane normal to the locomotion direction, \vec{n} in the three-dimensional space can thus be expressed as follows:

$$\vec{B}_{desired} = B_0 (\cos(2\pi ft) \vec{u} + \sin(2\pi ft) \vec{n} \times \vec{u}) \quad (4)$$

where B_0 is the magnitude of the electromagnetic field, f is the frequency of the desired electromagnetic field, and \vec{u} is the unit vector of the desired electromagnetic field plane in the externally driven electromagnetic system.

To achieve the desired steering or drilling motion, the calculated magnetic field must be mapped onto the applied currents of the magnetic coils. The aforementioned magnetic fields in (3) and (4) can be described again as the summation of the generated fields from each coil corresponding to the applied currents:

$$B_{desired} = \sum_1^n \tilde{B}_e i_e = B_e I \quad (5)$$

where \tilde{B}_e is the unit current vector field of the j -th coil [T/A] and B_e is the unit current matrix of the system, which has been explained in detail in our previous work [40]. Finally, the currents required to generate the desired electromagnetic field can be obtained by the following inverse electromagnetic field equation [45]:

$$I = B_e^\dagger B_{desired} \quad (6)$$

where B_e^\dagger denotes the pseudo-inverse of B_e .

In the case of drilling control, the current from the power supply is transmitted through the resonance control system to prevent a power drop due to induction at high frequencies [40]. A magnetic flux density of 30 mT was achieved at a rotational electromagnetic field frequency of 18–370 Hz. This results in a maximum force of 0.8 N and torque of 0.1125 mN·m (at 100 Hz) when drilling the thrombus.

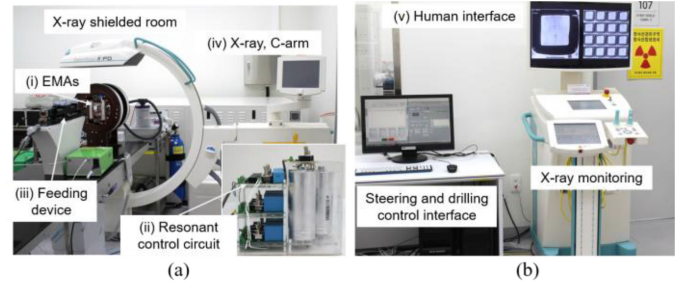


Fig. 4. Overview of the GHM control system. (a) X-ray shielded room where the experiment is conducted, which includes the (i) EMA system for steering and drilling control of the GHM, (ii) resonant control circuit, (iii) feeding device, and (iv) C-arm X-ray imaging device. (b) Interface for user control of the EMA system and monitoring experiments.

IV. EXPERIMENTAL RESULTS

A. Experimental Setup

From the perspective of the practical application of the completely controllable GHM for mechanical atherectomy, the control system is composed of five main components (as shown in Fig. 4): an EMA, a resonance control system, a guidewire feeding device, a monitoring system, and a remote control interface. The EMA comprises three pairs of Helmholtz coils placed along the three mutually perpendicular axes of the Cartesian coordinate system such that the maximum accessible workspace could accommodate the rats used in the animal experiments, as shown in Fig. 4(a). The coils were powered by three programmable power supplies (MX15, AMETEK, USA) with a maximum rated power of 15 kW and an accuracy of ± 0.1 V. The EMA was designed to generate a three-dimensional magnetic field with a maximum intensity of 30 mT for steering the GHM. The resonance control system was used to enhance the drilling performance of the GHM by compensating for the high inductor reactance of the coil at high operation frequencies (Fig. 4(a)). This could aid in maintaining a high current at a wide range of operation frequencies, making it possible to deliver a sufficiently high drilling torque for fast drilling. The back and forth driving motion of the GHM was remotely controlled by the motorized feeding device to advance the GHM in the automatic tracing mode.

To obtain visual feedback, optical cameras as well as a C-arm X-ray imaging system were used in this study. The optical camera was used to visualize the orientation and position of the GHM in the vascular phantom model. While the C-arm X-ray imaging system (Ziehm Vision RFD, Ziehm Imaging GmbH, Germany) was used to observe the GHM during the *in vivo* experiments as shown in Fig. 4(a).

A user interface was developed for steering, drilling, and achieving guidewire insertion control. Fig. 4(b) shows the control station of the GHM, which was located outside the X-ray shielded room, thereby protecting the clinician from radiation exposure. The drilling motion was controlled by the three resonant circuits and three NI DAQ USB-6351 boards to generate a powered rotating magnetic field with a maximum frequency of up to 370 Hz. The driving motion of the GHM associated with the

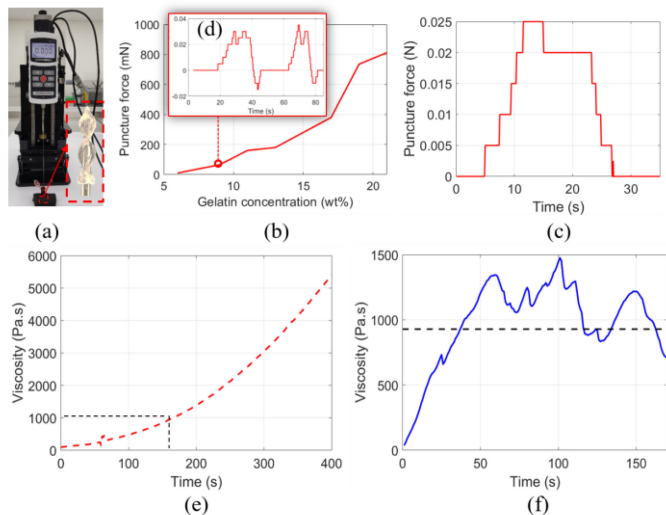


Fig. 5. (a) Experimental setup of required puncture force for penetrating the blood clot and gelatin. (b) Experimental results of puncture force requirement for gelatin with various concentrations, measured after one day of gelation. (c) Puncture force for penetrating the blood clot. (d) Puncture force for penetrating gelatin 9% (w/w), measured after setting for 3 minutes. (e) Measurement of gelatin 9% (w/w) viscosity against time. (f) Viscosity of blood clot.

130-mm Nitinol guidewire was controlled by the feeding device (included the motorized linear stage from Mitsumi and our homebuilt supporting parts). A flexible plastic sheath (Tygon, USA) with inner and outer diameters of 0.79 mm and 2.38 mm, respectively, was used as the guiding catheter.

B. Preparation of Artificial Thrombi

Artificial thrombi were prepared for both the phantom and the animal models. There are difficulties involved in embedding artificial thrombi in the animal model. For the *in vivo* creation of an artificial thrombus, the material needs to be injected in the liquid form; however, it should solidify sufficiently fast to ensure that the animal survives while conducting experiments. Moreover, this material should remain stationary inside the vessel of the animal during solidification.

To prepare and characterize the artificial thrombi, blood was first extracted from the rats, mixed with 1% gelatin (w/w), and then set for two days in a refrigerator. Thereafter, the viscosity of this mixture and the required puncture force were determined. Properties of the blood clot (i.e., the required puncture force and viscosity) are shown in Fig. 5(c) and (f). Considering the required puncture force of 25 mN, the blood clot is softer than calcified blood clots. During the investigation of the drilling performance of the GHM, gelatin (G2500, Sigma-Aldrich, Korea) was employed for preparing the artificial thrombi. It was discovered that 9% gelatin (w/w) exhibited physical properties similar to those of a blood clot in terms of viscosity and required puncture force, as shown in Fig. 5. The 9% gelatin (w/w) solution was heated in a microwave for 10 s and placed on a hot plate at 38° (above its melting point) for subsequent use in the *in vitro* and *in vivo* experiments.

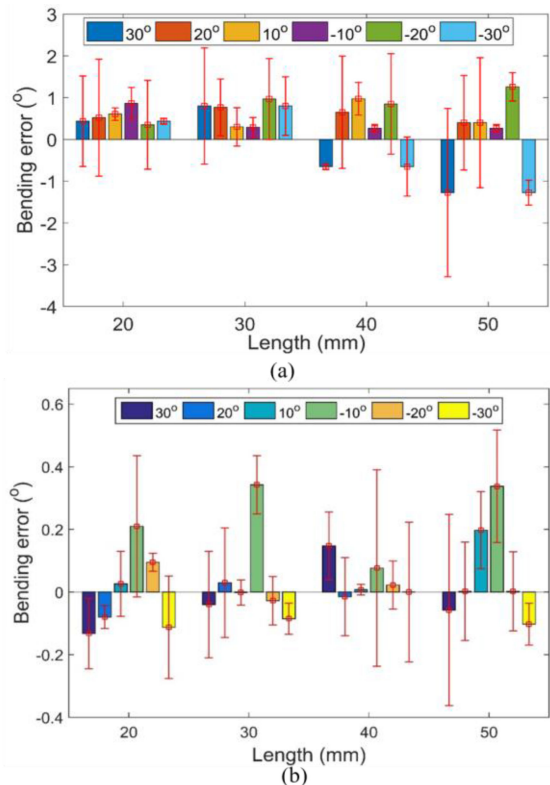


Fig. 6. Basic steering control and drilling test. Experimental results of (a) feedforward control and (b) feedback controls with various desired bending angles ($\pm 10^\circ$, $\pm 20^\circ$, and $\pm 30^\circ$) and guidewire lengths (20 mm, 30 mm, 40 mm, and 50 mm). (c) Drilling performance of the GHM evaluated through an artificial thrombus comprising 9% gelatin (w/w) in a cylindrical tube.

C. Characterization of Blood Clots and Gelatin

Gelatin solution samples with varied concentrations (w/w) of 6%, 9%, 11%, 13%, 15%, 17%, 19%, and 21%, which were set at room temperature for a day, were used for the puncture force test. Fig. 6(a) illustrates the experimental setup for the puncture force test. In this setup, a force gauge (series 5, MARK-10 Cor., USA) with an accuracy of 5 mN was affixed on the motorized linear stage and used to measure the puncture force for the proposed micro-driller attached at the needle tip. Fig. 5(b)–(d) demonstrate the measurement results of the required puncture force for gelatin against the blood clot.

For the viscosity test, a viscometer (Brookfield DV2T, Brookfield engineering laboratory, Inc., USA) with a sampling frequency of 1 Hz was used. The experimental results of gelatin's viscosity in terms of time are shown in Fig. 5(e), which represent the gelation process of gelatin itself. These results can be used for determining fabrication parameters of gelatin (gelation time and concentration) that are similar to blood clot properties by comparing the obtained values with the blood clot viscosity.

D. Steering Control and Drilling Test

Fig. 6(a) and 6(b) show the bending errors ($\gamma_d - \gamma_m$) obtained by the experiments (γ_m) and the desired value (γ_d) for the feedback and feedforward steering angle controls. The GHM deflections were tested by varying the desired steering angles by $\pm 10^\circ$, $\pm 20^\circ$, and $\pm 30^\circ$ for varied guidewire lengths of 20 mm, 30 mm, 40 mm, and 50 mm, respectively. The maximum bending error of the GHM for feedforward control is observed to be approximately 3° for the desired bending angle of 30° and guidewire length of 50 mm, as shown in Fig. 6(a). These results indicate that the bending model of the GHM does not precisely match the actual device. In the feedback controller, this bending error was recursively fed back to the PID controller, as shown in Fig. 6(b). The steering angle control performance for feedback control is significantly better than that for feedforward control, where bending errors are less than 0.5° (except for the case with a bending angle of 10° and length of 50 mm, which yielded a maximum error of 0.52°).

Drilling motion was tested in a cylindrical tube that was clogged with an artificial thrombus. This thrombus was composed of the gelatin solution with various concentrations, including 9%, 11%, and 15% (w/w). These thrombi were dyed green and set after 10 mins. The GHM was driven by the rotating magnetic field with a field strength of 15mT and an operating frequency of 100 Hz, respectively. The feeding velocity of the

GHM was set to 1.5 mm/s. Fig. 6(c) shows the drilling performance of the GHM in penetrating through an artificial thrombus with a length of 54 mm and comprising 9% (w/w) gelatin. The GHM drills through the artificial thrombus in approximately 48 s, and the drilling motion remains consistent throughout thrombus penetration. Also, the GHM drills through a thrombus with a length of 40 mm and comprising 11% (w/w) gelatin within 43 s. The magnetic torque induced by the enhanced rotating field is still sufficient to maintain the drilling motion. Finally, as validation of its revascularization performance, the GHM could drill through a 46-mm-long thrombus comprising 15% gelatin within 56 s; in this case, however, the drilling motion was partially obstructed and the guidewire was bent due to the hardness of the thrombus. This experiment is provided as Supplementary Video S1.

E. Navigation of the GHM in Vessel Phantom

The path-tracking and navigation performance of the GHM was assessed using a vessel phantom filled with deionized (DI) water and placed inside the workspace of the EMA system. The developed trajectory planning algorithm enables users to choose the desired path, which can be automatically generated after

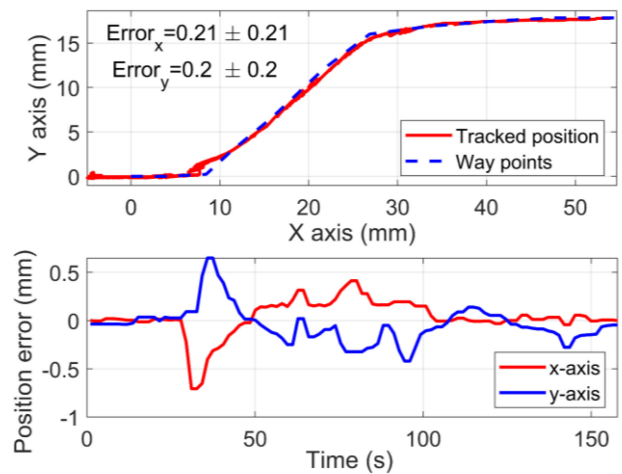


Fig. 7. 2D tracking in vessel phantom. Tracked position and position error of the GHM along a given path.

clicking a few points along the path to track the GHM. The algorithm creates a path according to the chosen points along with the vessel length and vessel angles that were recorded and preprocessed beforehand (pre-op image) [46], [47]. Fig. 4 shows the developed ENS and Fig. 3(a) depicts the block diagram of path-tracking control using feedforward and feedback control algorithms. At each point, information related to the current and subsequent positions was compared and utilized to generate the next steering angle and deduce the errors fed to the feedforward and feedback controllers. The algorithms, which receive data, process visual feedback and human commands, and communicate with peripheral devices, could be executed in real-time using LabVIEW (National Instruments, USA) and MATLAB software through MATLAB script nodes.

Fig. 7 depicts the tracked position and the tracking errors of the tip of the GHM; the root-mean-square error is approximately 0.2 mm and the maximum position error is lower than 0.7 mm when the feeding velocity, v_d , of the GHM is set to 0.3 mm/s.

F. In Vivo Experiment

The experiments were conducted in accordance with the ethical guidelines of the National Institute of Health and with the approval of the Chonnam National University Institutional Animal Care and Use Committee (CNU IACUC-YB-2019-78) review board. A tabletop anesthesia system (Harvard Apparatus, Harvard Bioscience Inc.) was used to maintain the rats in the anesthetized state during the procedure. A micropump (μ Flucon, AMED Inc., Korea) was used to pump the X-ray contrast medium (iohexol, Omnipaque 300, GE Healthcare, Korea) into the rats' aorta for evaluating the vessel shape. The formation of the artificial thrombi and the thrombus removal process was observed via X-ray monitoring.

Fig. 8(a) demonstrates the experimental procedure of removing a thrombus from the rat's abdominal aorta using the GHM. The steps involved in this procedure are listed as follows:

- 1) A 20G catheter was inserted into the lower part of the infrarenal aorta for injecting the contrast medium.

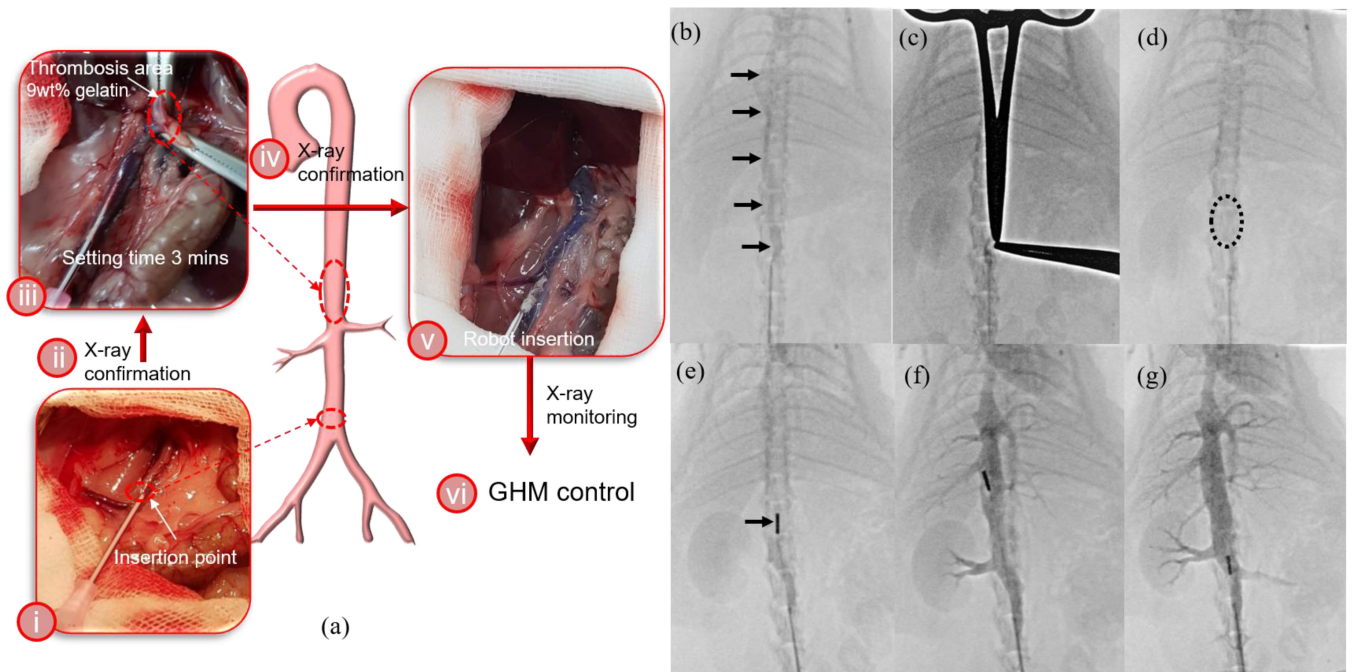


Fig. 8. (a) Thrombus removal in the rat. a. Experimental procedure for thrombus removal from the abdominal aorta of the rat. Shape of the abdominal aorta of rat #4 (b, arrows) before thrombus formation. Two forceps are clamped in the upper part of the infrarenal aorta and left renal artery (c), and the artificial thrombus is injected into this area. Thrombus formation after 3 min of gelation and removal of the forceps (d, dotted oval). The GHM reaches the thrombus area (e, arrow) and drills through the thrombus (f). (g) GHM is retracted.

- 2) The shape of the abdominal aorta was evaluated through angiography after injecting the contrast medium.
- 3) Forming the thrombus: 350 μ l of 9% (w/w) gelatin was injected from the lower part of the infrarenal aorta, while the upper part of the infrarenal aorta and the left renal artery was clamped in advance.
- 4) The formation of the artificial thrombus was observed through X-ray fluoroscopy before and after retrieving the forceps. The blockage of the contrast medium flow confirmed the formation of the thrombus.
- 5) The GHM was then inserted into the abdominal aorta through the same insertion point.
- 6) The GHM was driven to reach the thrombus, and thrombus removal was achieved using the guidewire and the ENS system.

After completing revascularization, the GHM was retrieved outside the rat body.

G. In Vivo Experimental Results

The thrombus removal performance in living rats was investigated to verify the clinical usability of the proposed method. The abdominal aorta of rats (males, 14 weeks old \pm 5 days) was chosen as an alternative for the human coronary artery, considering the similar vessel sizes (1.6–4.5 mm) [42], [44]. The rat was placed inside the workspace of the EMA system, where its abdomen was opened in advance under anesthetized conditions.

Revascularization procedures were successfully conducted for the remaining rats #4 and #5. For rats #3, #4, and #5,

the GHM could successfully drill through the thrombi without perforating the aortas. However, rat #3 was confirmed dead after the removal of artificial thrombus because of bleeding. For rats #4 and #5, Fibrin glue (Greenplast Q Prefilled Syringe Kit (2 mL) from GCPharma, Korea) was used after GHM insertion to stop the bleeding during the procedure. The success rate of mechanical atherectomy using the prototyped system was 100% for the well-prepared rats. The automatic guidance of the GHM toward the target thrombus was successful, and the helical robot demonstrated adequate drilling force. After thrombus removal, blood flow recovery could be monitored using angiography as shown in Fig. 8, through which the main artery was detected and heart-pumping movements were also observed clearly. This is definitive evidence of the recovery of cardiovascular functionality. After penetrating the thrombus, blood flow is recovered, and the motion of the helical robot is slightly skewed due to the recovered hemodynamics. In which, it is observed that the helical microrobot does not hit the wall of the vessel and we confirm that the designed system can be adequately working for this procedure. However, the resisting function of the assembled guidewire for the higher hemodynamic condition in large animal needs to be conquered further. Finally, the GHM returned to the catheter sheath and could be retrieved without further damage to the body. Thus, the risk involved in the procedure is effectively reduced when utilizing the micro-fabricated device.

Fig. 8(b)–(f) illustrate angiography images of one of the successful cases (case #4) corresponding to experimental procedures (ii), (iv), and (vi) in Section IV.F. The results of the complete mechanical thrombectomy procedure are provided in Supplementary Video S2.

TABLE II
SUMMARY OF *IN VIVO* EXPERIMENT RESULTS

| No. | Age | Successful in 1st thrombus formation | Successful in 2 nd thrombus formation | Successful in thrombus removal | Remark |
|-----|------------------|--------------------------------------|--|--------------------------------|--------|
| #1 | 14 weeks, 2 days | Leakage | Leakage | N/A | Death |
| #2 | 14 weeks, 1 day | Leakage | Yes | Yes | Death |
| #3 | 14 weeks, 4 days | Yes | N/A | Yes | Death |
| #4 | 14 weeks, 5 days | Yes | N/A | Yes | Alive |
| #5 | 14 weeks, 5 days | Yes | N/A | Yes | Alive |

Table II summarizes the *in vivo* experimental results. Among the five rats undergoing thrombus removal, rats #1 and #2 died during thrombus formation and rat #3 died after completion of the atherectomy. As the tested vessels are major arteries in rats, even a minimal amount of mishandling of the guidewire can cause severe vascular problems leading to death. Overall, the success rate of artificial thrombus formation was 60% in the first trial. For rats #1 and #2, the thrombi were not fully occluded in the abdominal aorta; a contrast medium leakage through the thrombus was observed in the angiography image corresponding to the first trial of thrombus formation. In these rats, the second trial of thrombus formation involved injecting 150 μ l of 9% gelatin at the same position. The thrombus could not be created in rat #1, but it was created in rat #2 during the second trial. However, both these rats died because of bleeding.

V. DISCUSSIONS AND CONCLUSION

In this study, we proposed a GHM for mechanical atherectomy in narrow vessels and validated its performance through *in vitro* and *in vivo* experiments. The developed prototype could perform efficient steering and drilling motions using the advanced ENS for a given angiography environment while maintaining its tip at the center of the vessel to avoid perforations.

The age of the CTO is considered an important factor in choosing the guidewire for penetrating CTO in PCI. Early-stage CTO is soft and can be easily pierced using thin guidewires or some wireless micro-drillers [43], [48]. However, aged CTO is considerably more difficult to penetrate without the use of a wireless micro-driller. For instance, the mean puncture force required for a six-week-old CTO is estimated to be 0.78 N [49]. Thus, the proposed GHM, a freely rotatable helical microrobot, can treat thrombi as well as aged lesions, because the maximum puncture force of the guidewire used (diameter of 0.152 mm) is 0.8 N. Nevertheless, a thicker or thinner guidewire would be needed for treating CTO of varied ages; the trade-off between puncture force and flexibility of the GHM needs to be considered when handling aged CTO. Furthermore, the remained debris after the procedure by using this device is expected to be smaller than those after the puncture device, owing to the drilling motion of the GHM. The methods developed in this work can be integrated with a catheter featuring a balloon for occlusion and suction of

the debris remaining after the removal process. Besides, drug therapy can also be employed after the procedure.

From the perspective of robotic therapeutics, helical micro- or milli-meter robots mimicking flagella and its screwing motion have been employed for small-sized robotic actuation in industrial and biomedical applications [50]. Despite recent advances in soft robot configurations and wireless actuation methodologies, practical applications of these robots, especially in a clinical setting, are still scarce owing to the complications in the fabrication of these small-sized devices, insufficient driving power transmission, and the difficulty of visual feedback control. This study improved the practical applicability of high-powered guide-wired helical millirobots for mechanical atherectomy in cardiovascular interventions that enable autonomous therapeutics without any contact between clinicians and patients. Moreover, safe retrieval of the therapeutic tool after the completion of the procedure is another benefit of the proposed method, as compared to previously developed microrobots. As the materials and apparatus utilized for this study are already available in clinical sites, further improvements in the applicability of the GHM can be achieved using the animal model preparation described herein. Additional efforts are required to develop an efficient and safe mechanical atherectomy robot.

While driving the GHM with an orientation of under 40°, the model could perform fairly similar to the experimental results. However, in case of an orientation of 40° or a maximum of 53°, the model demonstrated a larger error; the maximum error was 8.5°. In addition, at a small desired angle (< 5°) and a weak applied field, the GHM occasionally caused vibrations (Fig. 7(b)) owing to its free bending angle. Therefore, to improve posture control accuracy and achieve stable motion, an accurate guidewire string model and an advanced control method will be incorporated with fully 3D imaging devices and posture feedback. Moreover, a fracture at the 3D printed portion of the device was occasionally observed during the insertion of the GHM. A stainless steel helical robot body fabricated using micro-machining techniques is expected to be the next version of the proposed GHM, which will minimize device fractures during the procedure.

Finally, the *in vivo* experimental results prove that the proposed microrobot represents an advancement in the thrombus removal process for PCI, in terms of its precise controllability and efficient removal of blockages in a narrow vessel. Future research should consider clinical evaluations using a large animal with a scaled-up ENS system to realize more efficient medical microrobots with higher throughputs.

REFERENCES

- [1] K. Kearney *et al.*, "Update on the management of chronic total occlusions in coronary artery disease," *Curr. Atheroscler. Rep.*, vol. 19, no. 4, 2017. [Online]. Available: <https://link.springer.com/article/10.1007/s11883-017-0655-0>
- [2] J. H. Rogers and J. R. Laird, "Overview of new technologies for lower extremity revascularization," *Circulation*, vol. 116, no. 18, pp. 2072–2085, 2007.
- [3] A. T. L. Ong and P. W. Serruys, "Complete revascularization: Coronary artery bypass graft surgery versus percutaneous coronary intervention," *Circulation*, vol. 114, no. 3, pp. 249–255, 2006.

- [4] C. Collet *et al.*, "Left main coronary artery disease: Pathophysiology, diagnosis, and treatment," *Nat. Rev. Cardiol.*, vol. 15, no. 6, pp. 321–331, 2018.
- [5] Y. P. Gobin *et al.*, "MERC1: A phase I study of mechanical embolus removal in cerebral ischemia," *Stroke*, vol. 35, no. 12, pp. 2848–2853, 2004.
- [6] S. Takahashi *et al.*, "New method to increase a backup support of a 6 french guiding coronary catheter," *Catheter Cardiovasc. Interv.*, vol. 63, no. 4, pp. 452–456, 2004.
- [7] B. C. Campbell *et al.*, "Endovascular stent thrombectomy: The new standard of care for large vessel ischaemic stroke," *LANCET Neurol.*, vol. 14, no. 8, pp. 846–854, 2015.
- [8] A. S. Turk *et al.*, "Initial clinical experience with the ADAPT technique: A direct aspiration first pass technique for stroke thrombectomy," *J. Neurointerv. Surg.*, vol. 6, no. 3, pp. 231–237, 2014.
- [9] R. Erbel *et al.*, "High-Frequency rotablation of occluded coronary artery during heart catheterization," *Cathet. Cardiovasc. Diagn.*, vol. 17, no. 1, pp. 56–58, 1989.
- [10] M. E. Bertrand *et al.*, "Percutaneous transluminal coronary rotary ablation with rotablator (European experience)," *Amer. J. Cardiol.*, vol. 69, no. 5, pp. 470–474, 1992.
- [11] N. I. Akkus and A. Abdulbaki, "Rotational atherectomy in peripheral arterial interventions," in *Textbook of Catheter-Based Cardiovascular Interventions*, P. Lanzer, ed. Cham, Switzerland: Springer, 2018, pp. 1377–1388.
- [12] J. P. Pigott, M. L. Raja, and T. Davis, "A multicenter experience evaluating chronic total occlusion crossing with the wildcat catheter (the CONNECT study)," *J. Vasc. Surg.*, vol. 56, no. 6, pp. 1615–1621, 2012.
- [13] C. Wissgott, P. Kamusella, and R. Andresen, "Recanalization of acute and subacute venous and synthetic bypass-graft occlusions with a mechanical rotational catheter," *Cardiovasc. Intervent. Radiol.*, vol. 36, no. 4, pp. 936–942, 2013.
- [14] S. R. Duc *et al.*, "Recanalization of acute and subacute femoropopliteal artery occlusions with the rotarex catheter: One year follow-up, single center experience," *Cardiovasc. Intervent. Radiol.*, vol. 28, no. 5, pp. 603–610, 2005.
- [15] S. Shafique *et al.*, "Recanalization of infrainguinal vessels: Silverhawk, laser, and the remote superficial femoral artery endarterectomy," *Semin. Vasc. Surg.*, vol. 20, no. 1, pp. 29–36, 2007.
- [16] P. Kumar and M. S. Levy, "Radiation exposure in the cardiac catheterization lab," *Catheter Cardiovasc. Interv.*, vol. 82, no. 1, pp. 17–18, 2013.
- [17] M. S. Choi *et al.*, "Comparison of magnetic navigation system and conventional method in catheter ablation of atrial fibrillation: Is magnetic navigation system is more effective and safer than conventional method?," *Korean Circ. J.*, vol. 41, no. 5, pp. 248–252, 2011.
- [18] A. M. Kim *et al.*, "Impact of remote magnetic catheter navigation on ablation fluoroscopy and procedure time," *PACE - Pacing Clin. Electrophysiol.*, vol. 31, no. 11, pp. 1399–1404, 2008.
- [19] T. M. Patel *et al.*, "Comparison of robotic percutaneous coronary intervention with traditional percutaneous coronary intervention: A propensity score-matched analysis of a large cohort," *Circ. Cardiovasc. Interv.*, vol. 13, no. 5, pp. 1–6, May 2020.
- [20] P. Destrebecq *et al.*, "Robotizable module for driving an elongated flexible medical member, medical robot and system including such a module," US 2020/0254218 A1, 2020.
- [21] S. A. Virk and S. Kumar, "Remote magnetic versus manual catheter navigation for atrial fibrillation ablation: A meta-analysis," *Circ. Arrhythmia Electrophysiol.*, vol. 12, no. 10, pp. 1–3, 2019.
- [22] J. Chakravarti and S. V. Rao, "Robotic assisted percutaneous coronary intervention: Hype or hope?," *J. Amer. Heart Assoc.*, vol. 8, no. 13, pp. 1–4, 2019.
- [23] A. D. Losey *et al.*, "Magnetically assisted remote-controlled endovascular catheter for interventional MR imaging: In vitro navigation at 1.5 t versus X-ray fluoroscopy," *Radiology*, vol. 271, no. 3, pp. 862–869, 2014.
- [24] K. R. J. Chun *et al.*, "Catheter ablation - New developments in robotics," *Herz*, vol. 33, no. 8, pp. 586–589, 2008.
- [25] F. Kiemeneij *et al.*, "Use of the stereotaxis niobe magnetic navigation system for percutaneous coronary intervention: Results from 350 consecutive patients," *Catheter Cardiovasc. Interv.*, vol. 71, no. 4, pp. 510–516, 2008.
- [26] E. S. Gang *et al.*, "Dynamically shaped magnetic fields: Initial animal validation of a new remote electrophysiology catheter guidance and control system," *Circ. Arrhythmia Electrophysiol.*, vol. 4, no. 5, pp. 770–777, 2011.
- [27] B. L. Nguyen *et al.*, "Non-fluoroscopic transeptal catheterization during electrophysiology procedures using a remote magnetic navigation system," *J. Atr. Fibrillation*, vol. 6, no. 4, pp. 6–9, 2013.
- [28] Z. Shaikh, M. Eilenberg, and T. Cohen, "The Amigo remote catheter system: From concept to bedside," *J. Innov. Card. Rhythm Manag.*, vol. 8, no. 8, pp. 2795–2802, 2017.
- [29] T. Datino *et al.*, "Arrhythmia ablation using the amigo robotic remote catheter system versus manual ablation: One year follow-up results," *Int. J. Cardiol.*, vol. 202, pp. 877–878, 2016.
- [30] M. Valderrábano *et al.*, "Robotic catheter ablation of left ventricular tachycardia: Initial experience," *Heart Rhythm*, vol. 8, no. 12, pp. 1837–1846, 2011.
- [31] W. Saliba *et al.*, "Atrial fibrillation ablation using a robotic catheter remote control system. Initial human experience and long-term follow-up results," *J. Amer. Coll. Cardiol.*, vol. 51, no. 25, pp. 2407–2411, 2008.
- [32] C. Chautems and B. J. Nelson, "The tethered magnet: Force and 5-DOF pose control for cardiac ablation," in *Proc. IEEE Int. Conf. Robot. Autom.*, pp. 4837–4842, 2017.
- [33] S. Jeong *et al.*, "Feasibility study on magnetically steerable guidewire device for percutaneous coronary intervention," *Int. J. Control. Autom. Syst.*, vol. 15, no. 1, pp. 473–479, 2017.
- [34] J. Sikorski *et al.*, "Vision-Based 3-D control of magnetically actuated catheter using bigmag - An Array of mobile electromagnetic coils," *IEEE/ASME Trans. Mechatronics*, vol. 24, no. 2, pp. 505–516, Apr. 2019.
- [35] J. Sikorski *et al.*, "The ARMM system: An optimized mobile electromagnetic coil for non-linear actuation of flexible surgical instruments," *IEEE Trans. Magn.*, vol. 55, no. 9, pp. 1–9, Sep. 2019.
- [36] M. Schiemann *et al.*, "Vascular guide wire navigation with a magnetic guidance system: Experimental results in a phantom," *Radiology*, vol. 232, no. 2, pp. 475–481, 2004.
- [37] S. Jeon *et al.*, "A magnetically controlled soft microrobot steering a guidewire in a three-dimensional phantom vascular network," *Soft Robot.*, vol. 6, no. 1, pp. 54–68, 2019.
- [38] F. Settecase *et al.*, "Magnetically-assisted remote control (MARC) steering of endovascular catheters for interventional MRI: A model for deflection and design implications," *Med. Phys.*, vol. 34, no. 8, pp. 3135–3142, 2007.
- [39] M. Ilami *et al.*, "Magnetic needle steering in soft phantom tissue," *Sci. Rep.*, vol. 10, no. 1, pp. 1–12, 2020.
- [40] K. T. Nguyen *et al.*, "High-frequency and High-powered electromagnetic actuation system utilizing Two-stage resonant effects," *IEEE/ASME Trans. Mechatronics*, vol. 25, no. 5, pp. 2398–2408, Oct. 2020.
- [41] H. Choi *et al.*, "Simplified electromagnetic actuation system for three dimensional locomotive and drilling microrobot," in *Proc. Inst. Mech. Eng. Part C: J. Mech. Eng. Sci.*, vol. 229, no. 13, pp. 2443–2454, 2015.
- [42] G. Bin Jang *et al.*, "A spiral microrobot performing navigating linear and drilling motions by magnetic gradient and rotating uniform magnetic field for applications in unclogging blocked human blood vessels," *IEEE Trans. Magn.*, vol. 51, no. 11, May 2015. [Online]. Available: <https://ieeexplore.ieee.org/abstract/document/7112155/>
- [43] S. Lee *et al.*, "Fabrication and characterization of a magnetic drilling actuator for navigation in a three-dimensional phantom vascular network," *Sci. Rep.*, vol. 8, no. 1, pp. 1–9, 2018.
- [44] J. T. Dodge *et al.*, "Lumen diameter of normal human coronary arteries. Influence of age, sex, anatomic variation, and left ventricular hypertrophy or dilation," *Circulation*, vol. 86, no. 1, pp. 232–246, 1992.
- [45] K. T. Nguyen *et al.*, "Regularization-based independent control of an external electromagnetic actuator to avoid singularity in the spatial manipulation of a microrobot," *Control Eng. Pract.*, vol. 97, no. 4, Apr. 2020. Art. no. 104340.
- [46] J. Kim *et al.*, "A novel Tip-positioning control of a magnetically steerable guidewire in sharply curved blood vessel for percutaneous coronary intervention," *Int. J. Control. Autom. Syst.*, vol. 17, no. 8, pp. 1–14, 2019.
- [47] P. B. Nguyen *et al.*, "Real-time microrobot posture recognition via biplane X-ray imaging system for external electromagnetic actuation," *Int. J. Comput. Assist. Radiol. Surg.*, vol. 13, no. 11, pp. 1843–1852, 2018.
- [48] S. Jeong *et al.*, "Enhanced locomotive and drilling microrobot using precessional and gradient magnetic field," *Sensors Actuators, A. Phys.*, vol. 171, no. 2, pp. 429–435, 2011.
- [49] T. T. A. *et al.*, "A novel method for the measurement of proximal fibrous cap puncture force in chronic total occlusions: The effect of increasing age," *EuroIntervention*, vol. 6, no. 8, pp. 997–1002, 2011. [Online]. Available: <https://europepmc.org/article/med/21330249>
- [50] J. J. Abbott *et al.*, "How should microrobots swim?," *Int. J. Rob. Res.*, vol. 28, no. 11–12, pp. 1434–1447, 2009.